Research Article

Mohammad Reza Karami, Babak Jaleh*, Mahtab Eslamipanah, Atefeh Nasri, and Kyong Yop Rhee*

Design and optimization of a TiO_2/RGO-supported epoxy multilayer microwave absorber by the modified local best particle swarm optimization algorithm

https://doi.org/10.1515/ntrev-2023-0121
received December 30, 2022; accepted August 21, 2023

Abstract: Microwave absorbers have many applications in medical, industrial, and military devices. Polymeric composites including carbon-based filler can be used as lightweight absorbers with high electromagnetic (EM) wave absorption performance. Hence, multilayer microwave absorbers were designed using titanium dioxide (TiO_2)/reduced graphene oxide (RGO)/epoxy nanocomposites with different weight percentages manufactured using refluxing and annealing methods. The characterization of nanocomposite indicated thin layers of TiO_2/RGO as divided sheets in epoxy. The EM properties of the nanocomposites were examined using the Nicolson-Ross-Weir (NRW) detection method. The S-parameters were measured using PNA-N5222A Microwave Network Analyzer. The multilayer absorber software was designed based on the modified local best particle swarm optimization algorithm by MATLAB software, in which the material and thickness of layers were optimized with two cost functions in X-band frequencies. The first cost function seeks to reach the best absorption bandwidth, and the second cost function seeks to reach the maximum average return loss (RL) of the frequency range of 8.2–12.4 GHz. A maximum bandwidth with an RL of less than −12.81 dB was obtained with a thickness of 2.4 mm. A maximum average RL of −22.1 dB was obtained with a thickness of 2.6 mm. The maximum absorption peak was observed with a thickness of 2.5 mm with −62.82 dB at a frequency of 10.86 GHz.

* **Corresponding author: Babak Jaleh,** Department of Physics, Faculty of Science, Bu-Ali Sina University, 65174, Hamedan, Iran, e-mail: jaleh@basu.ac.ir
* **Corresponding author: Kyong Yop Rhee,** Department of Mechanical Engineering, Kyung Hee University, 17104 Yongin, Republic of Korea, e-mail: rheeky@khu.ac.kr
Mohammad Reza Karami, Mahtab Eslamipanah, Atefeh Nasri: Department of Physics, Faculty of Science, Bu-Ali Sina University, 65174, Hamedan, Iran

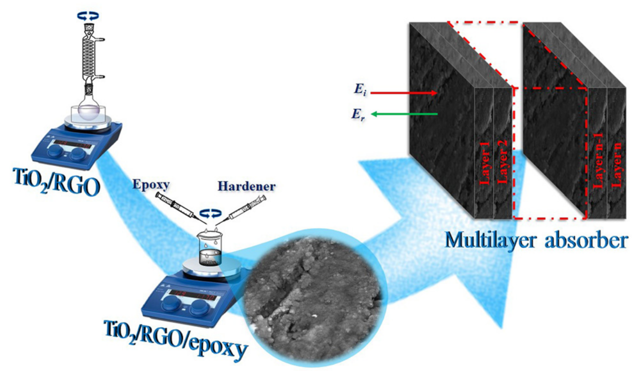

Graphical abstract

Keywords: graphene oxide, TiO_2 nanoparticles, multilayer microwave absorber, particle swarm optimization algorithm

1 Introduction

Developing electronic devices such as wireless telecommunication, radar systems, and local networks has recently led to electromagnetic (EM) wave radiation at different frequencies. Although electronic devices can simplify human life, the EM wave radiation of these devices is a serious environmental problem because it can damage the surrounding electronic devices and harm human health. Hence, efficient approaches must be investigated to control EM pollution effectively [1,2]. In electronic devices, the interference effect of neighboring systems and unwanted internal reflections may create external noises that cause problems in their operation. Therefore, EM absorbers can control those problems by the undesired waves and interferences. Nowadays, EM absorbers have many applications in improving EM compatibility and EM interference problems. By removing unwanted waves, they reduce environmental pollution and improve the performance of electronic devices [3,4].

For this purpose, nanostructures have been introduced as EM wave absorbers. To achieve highly efficient EM absorbers, two significant steps can be followed [5–10]: (i) designing compounds with particular EM coefficients and (ii) creating the maximum impedance matching, which is obtained by calculating the optimal thickness and arrangement of the layers. This multilayer absorber has better performance than a single-layer absorber. The higher the impedance matching, the less the reflection from the outer layer, and the more power of the radiation wave entering the absorbing medium, and by passing through it, the possibility of EM wave absorption increases.

Conductive polymer-based composites, which consist of polymers and conductive fillers, have been widely used for EM removal because of their considerable properties of high flexibility, lightweight nature, compatibility, good chemical stability, and low-cost processing [11,12]. Epoxy resin is widely used in electronic devices because of its lightweight, thermal stability, mechanical features, simple processing, and corrosion resistance. It can be used as an affordable and available matrix to fabricate EM-absorbing materials [11–14]. Furthermore, polymeric composites with carbon-based fillers, such as carbon nanotubes, carbon black, and graphene, have exhibited excellent EM wave attenuation performance due to their unique electronic and mechanical features [15]. Carbon-based absorbing materials possess high complex permittivity values, outstanding thermal stability, and lightweight [16]. To attain affordable and light absorbers, graphene-based compounds are well known as promising candidates [17]. Graphene, which can be produced through facile chemical processing of graphite, is a two-dimensional lattice of single-layer carbon atoms. It is particularly attractive as an excellent EM wave-absorbing material, especially in its oxide forms, due to its high specific surface area and dielectric constant [18–20]. Graphene oxide (GO) is a graphene nanosheet decorated with oxygen functional groups, such as epoxy, hydroxyl, and carboxyl groups. GO sheets include hexagonal ring-based carbon network having both sp^2 hybridized and sp^3 hybridized carbons [21]. Reduced graphene oxide (RGO), fabricated by removing the oxygen groups of GO, has been introduced to improve EM absorption. This improvement in EM absorption is ascribed to the defects and functional groups [22–24]. Defects and functional groups can enhance impedance-matching characteristics and rapid energy transitions from contiguous states to the Fermi level. However, graphene materials are non-magnetic, and their EM absorption ability is due to their dielectric loss. In addition, the permittivity and permeability of graphene materials do not balance together, leading to bad impedance matching. The composition of graphene materials with other nanostructures can improve their absorption capability [13].

Titanium dioxide (TiO_2) is a standard semiconductor metal oxide with wide applications due to its outstanding advantages such as nontoxicity, affordability, chemical stability, good dielectric properties, and high refractive index. It has a band gap of 3–3.2 eV and is available in three polymorphic crystalline forms: anatase, rutile, and brookite. Its low dielectric loss and high dielectric constant make it applicable as a nanofiller in a polymeric matrix for EM absorption [25–30].

The particle swarm optimization (PSO) algorithm is a random optimization technique inspired by the social behavior of bird herding and fish training [31,32]. This population-based self-adaptive algorithm has been used for many system problems. Since the order and thickness of the layers are significant in multilayer absorbers and the change in each one causes a change in absorber's performance, its optimization is critical. Multi-objective optimizers are used in designing and manufacturing multilayer absorbers, the most common of which are the genetic algorithm and PSO algorithm [7,33–35]. In this work, the modified local best particle swarm optimization (MLPSO) is used, a modified version of PSO, because it has high speed and accuracy and is easy to implement.

Hence, in this work, the TiO_2/RGO was synthesized using refluxing and thermal reduction methods and then dispersed in epoxy resin as filler *via* the stirring method. The EM features of the as-prepared nanocomposites (the complex permittivity and permeability coefficients) were perused using the Nicolson-Ross-Weir (NRW) method of the ASTM D5568-14, in which the samples were placed in the rectangular waveguide setup. Their S-parameters in the microwave X-band frequency range (8.2–12.4 GHz) were measured by the PNA N5222A microwave network analyzer. The MLPSO algorithm was used to design a multilayer absorber, in which the material and thickness of layers were optimized with two cost functions in X-band frequencies. The optimal values of average return loss (RL) of −22.1 dB and absorption peak of −62.82 dB were acquired with the thickness of 2.6 and 2.5 mm, respectively. Figure 1 illustrates a flowchart of the design and optimization process of the multilayer absorber.

2 Experimental

2.1 Materials and instrumentation

Chemical materials (powdered flake graphite, sodium nitrate, sulfuric acid, and potassium permanganate) to synthesize GO

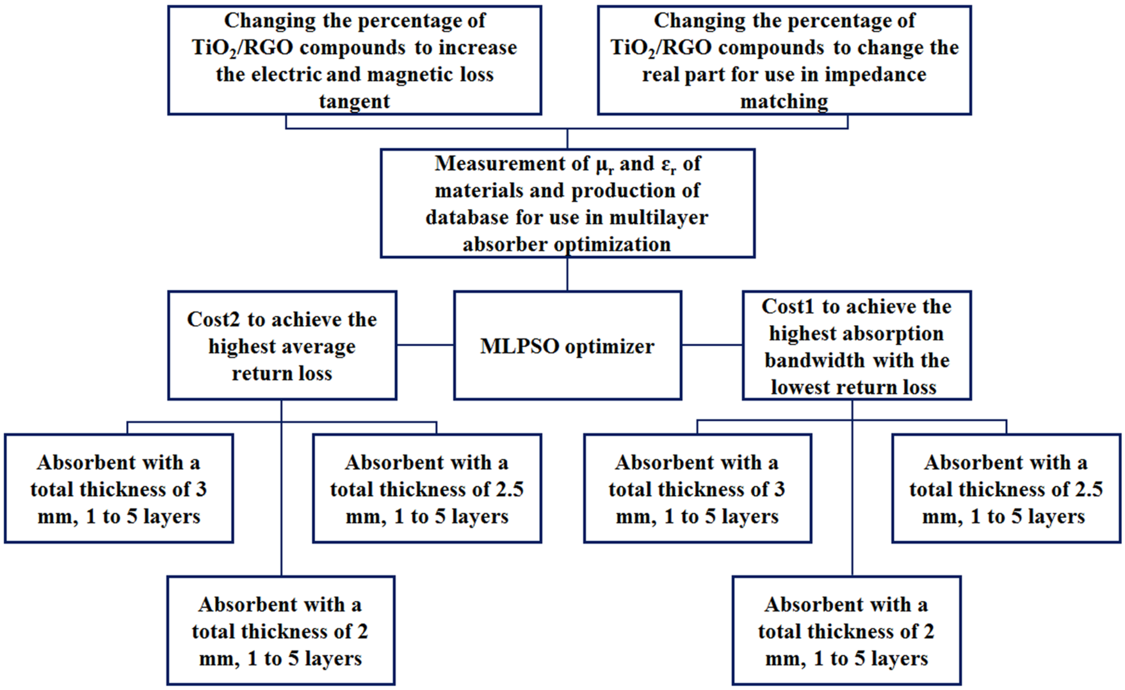

Figure 1: Flowchart showing the steps of design and optimization.

with high purity were purchased from the Merck company. TiO_2 nanoparticles (TiO_2 NPs), including biphasic anatase and rutile phases with a ratio of 80 to 20, were prepared from Degussa Co. (Germany). Epoxy resins with the commercial names resin 577 and hardener 567 were provided by the composite materials Co. (Turkish) supplier. X-ray diffraction (XRD, Italstructure, ADP200) patterns in 2θ degree range of 10–80° were performed to identify the crystalline phases present in the samples. Fourier transform infrared spectroscopy (FT-IR, Thermo Nicolet) was performed to detect the functional groups of the sample. Scanning electron microscopy (SEM, TSCAN) images were used to characterize the surface features and evaluate the morphological changes. The EM properties of the materials were calculated *via* an N5222A PNA Microwave Network Analyzer. Complex permittivity and permeability coefficients were calculated to measure the amount of reflection and transmission of microwave waves from the materials.

2.2 TiO_2/RGO/epoxy nanocomposite fabrication

GO nanosheets were synthesized *via* the oxidation of graphite through Hummer's method [36]. To fabricate the GO–TiO_2 nanocomposite, 0.03 g of GO and 0.03 g of TiO_2 NPs were separately dispersed in 100 ml of deionized water under sonication for 45 min to acquire homogenous suspensions. TiO_2 suspension was then added to the GO suspension. The GO–TiO_2 suspension was refluxed for 10 h at 80°C. An annealing method was used to prepare the RGO–TiO_2 nanocomposite, in which the GO–TiO_2 suspension was dried at 180°C for 3 hours. Different weight percentages of 7RGO:3TiO_2, 3RGO:7TiO_2, and 5RGO:5TiO_2 were fabricated. These nanocomposites were added to epoxy resin with a specific weight ratio as shown in Table 1 to prepare TiO_2-RGO-epoxy. The ingredients were mixed well for 20 min in 1.5 ml of ethanol using stirrer and poured into the mold. The samples were fabricated in a size of 10.1 × 22.8 × 3 and 10.1 × 22.8 × 2 mm^3. Figure 2 illustrates the TiO_2/RGO/epoxy nanocomposite preparation setup.

Table 1: Amount of material used for the preparation of TiO_2/RGO/epoxy nanocomposite

Sample name	TiO_2 (mg)	GO (mg)	RGO (mg)	Epoxy (mg)
S1	750	—	—	750
S2	—	355	—	750
S3	—	750	—	750
S4	225	525	—	750
S5	375	375	—	750
S6	525	225	—	750
S7	525	—	225	750
S8	375	—	375	750
S9	225	—	525	750

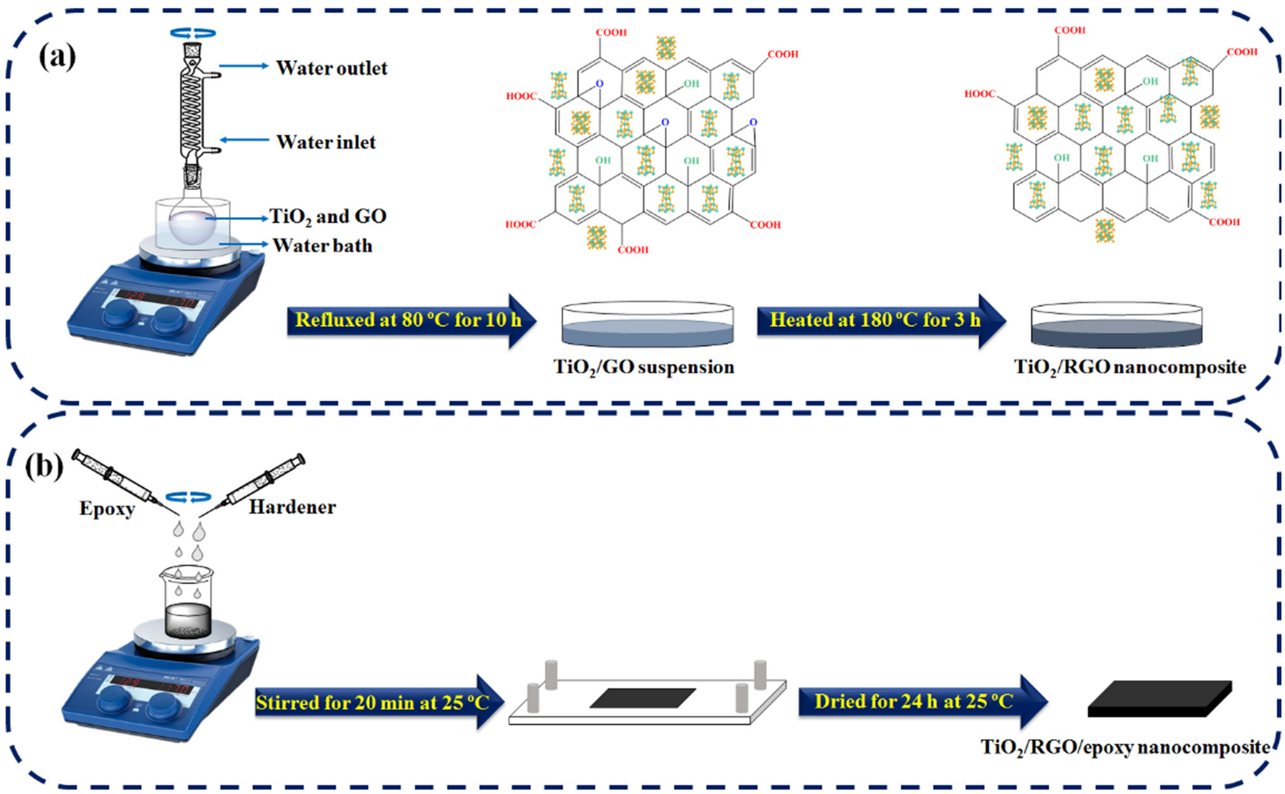

Figure 2: Schematic of the preparation of (a) TiO_2/RGO and (b) TiO_2/RGO/epoxy nanocomposites.

2.3 MLPSO

The PSO is a population-based self-adaptive algorithm with inherent parallelism, introduced in 1995 by Kennedy and Eberhart [32]. It is a global random optimization technique inspired by the social behavior of bird flocking and fish schooling. Because PSO has high speed, good convergence, and easy implementation, this algorithm is widely used in different optimization problems. MLPSO is one of the versions of PSO that prevents premature convergence of PSO and increases its accuracy. This method divides society into several local groups that do not overlap. In PSO, the random solutions are particles with a velocity in the search space that fly through a hyper-dimensional search space. In addition, the velocity and position of each particle update based on its best position in the search space [33]. Each particle is considered a point of the D-dimensional search space, and the ith particle is introduced by $x_i = (x_{i1}, x_{i2}, \ldots, x_{iD})$. The best previous position and velocity of the ith particle are demonstrated as $p_i = (p_{i1}, p_{i2}, \ldots, p_{iD})$ and $v_i = (v_{i1}, v_{i2}, \ldots, v_{iD})$, respectively. The D-dimensional vector of $p_g = (p_{g1}, p_{g2}, \ldots, p_{gD})$ is shown to be the best particle in the population [37]. If the g index shows the best particle in the population, the velocity and position are acquired by the following equations [33,38]:

$$v_i(d+1) = \omega v_i(d) + c_1 r \text{ and } (p_i(d) - x_i(d)) + c_2 r \text{ and } (p_g(d) - x_i(d)), \quad (1)$$

$$x_i(d+1) = x_i(d) + v_i(d+1), \quad (2)$$

where $v_i(d)$ and $x_i(d)$ illustrate the velocity and position of the ith particle, respectively, rand is a uniformly distributed random number between 0 and 1, and ω is the inertia weight. At the same time, c_1 and c_2 have denominated acceleration constants. The PSO algorithm is based on two versions of the global neighborhood (g-best) and local neighborhood (l-best). The aforementioned equations describe the gbest version of the PSO. For the lbest version, $p_g(d)$ should be changed to $p_l(d)$. Although the PSO algorithm is facile and computationally effective, its efficiency is unsatisfactory in solving complex multimodal optimization problems. Hence, modifying the PSO algorithm can improve its efficiency [33].

Quick convergence in solving complex multimodal problems is the major imperfection of PSO-based algorithms. Local PSO spans a wider search space; however, it has slow convergence. An MLPSO solution has been presented to prevent local optimum traps in complex search environments, in which neighborhoods do not overlap. Therefore, trapping the particle of a neighborhood into a locally optimized problem will not affect the other neighborhoods. Furthermore, one particle can only trap *via* each local optimum, increasing the chance of finding a global optimum by population [33].

2.4 Transmission line theory

Transmission line theory clarifies the results in terms of the transmitted/reflected waves, which was used to describe the electrical properties of nanocomposites. When a microwave enters into a nanocomposite consisting of absorber materials, the RL value can be acquired through the transmission line theory by the following equation [39–43]:

$$\mathrm{RL(dB)} = 20\log(\Gamma), \tag{3}$$

$$\Gamma = \frac{Z_{\mathrm{in}} - Z_0}{Z_{\mathrm{in}} + Z_0}, \tag{4}$$

$$Z_{\mathrm{in}} = Z_0\sqrt{\frac{\mu_{\mathrm{r}}}{\varepsilon_{\mathrm{r}}}}\tanh\left[j\left(\frac{2\pi df}{c}\right)\sqrt{\mu_{\mathrm{r}}\varepsilon_{\mathrm{r}}}\right], \tag{5}$$

where Γ is the interface reflection coefficient, and Z_{in} and Z_0 are the input impedance at the accessible space/nanocomposite interface and the intrinsic impedance of free space, respectively. In addition, μ_{r}, ε_{r}, and d are the complex relative permeability, complex relative permittivity, and thickness of the sample. f and c also show the microwave frequency and velocity of light in a vacuum. j is the complex constant ($j = \sqrt{-1}$). The microwave absorbent of a multilayer sample for normal incidence was calculated by the following equation [44,45]:

$$z_1 = \eta_1\frac{z_2 + \eta_1\tanh(k_1d_1)}{\eta_1 + z_2\tanh(k_1d_1)}, \tag{6}$$

$$z_n = \eta_n\frac{z_{n+1} + \eta_n\tanh(k_nd_n)}{\eta_n + z_{n+1}\tanh(k_nd_n)}, \tag{7}$$

where Z_n is the input impedance of the nth layer, and η_n and k_n are the impedance and propagation constant of the nth layer, respectively.

$$\eta_n = \eta_0\sqrt{\frac{\mu_{rn}}{\varepsilon_{rn}}}, \tag{8}$$

$$k_n = j\omega(\mu_0\varepsilon_0\mu_{rn}\varepsilon_{rn})^{1/2} = \frac{j2\pi}{\lambda}\sqrt{\mu_{rn}\varepsilon_{rn}}, \tag{9}$$

where ω and λ are the radian frequency and wavelength, respectively, and μ_{rn} and ε_{rn} are the complex relative permeability and complex relative permittivity of the nth layer, respectively. Accordingly, the multilayer absorbent possesses the RL as follows:

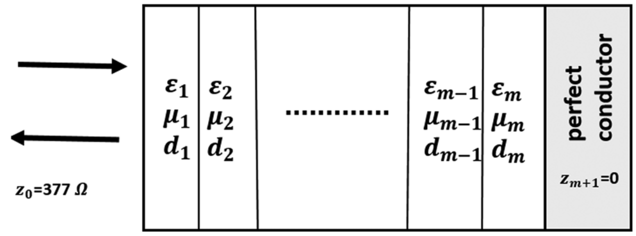

Figure 3: Multilayer absorber configuration.

$$\mathrm{RL(dB)} = 20\log\left(\frac{Z_{\mathrm{in}}(n) - Z_0}{Z_{\mathrm{in}}(n) + Z_0}\right) \tag{10}$$

Figure 3 shows a brief explanation of the multilayer absorber configuration.

3 Results and discussion

3.1 Materials' characterization

XRD analysis was deployed to study the crystalline structure and phase composition. As shown in Figure 4, the samples' XRD spectra confirm the nanocomposite's successful formation.

The XRD spectrum of the pure epoxy presents a wide diffraction peak (Figure 4(a)), indicating the amorphous phase of the epoxy resin. Figure 4(b) show sharp peaks at 25.4°, 37.9°, 48.2°, 54°, 55°, 62.8°, 70.4°, and 75.3°, assigned to the anatase phase (81%) of TiO_2. The diffraction peaks at 27.5° and 68.9° can be assigned to the rutile phase (19%), indicating that the main phase of TiO_2 NPs is anatase [46]. The crystalline size of the TiO_2 NPs is found to be 24.7 nm, calculated by Scherer's formula and full width at half maximum of the (101) peak [47]. The peak at 10.9° (Figure 4(b)) is associated with the formation of the GO owing to graphite oxidation. There is a broad characteristic peak at 16–24.1°, which is attributed to the single layer of the RGO in the spectrum corresponding to the TiO_2/RGO (30:70) (Figure 4(c)) [48–50]. Therefore, it can be concluded that the GO powder was incompletely converted to RGO. Moreover, the peaks of TiO_2 NPs show lower intensity compared to the spectrum of TiO_2/GO (Figure 4(b)) due to the immobilization of the RGO surface. Figure 3(d) presents the XRD pattern of TiO_2/RGO/epoxy (30:70:50).

Figure 5 shows the FT-IR spectra of TiO_2/GO and TiO_2/RGO nanocomposites. A wideband appeared in the 855–440 cm^{-1} range, indicating stretching vibrations of Ti–O in Ti–O–Ti bands [51–53]. The different peaks appearing at 1,546 and 1,694 cm^{-1}

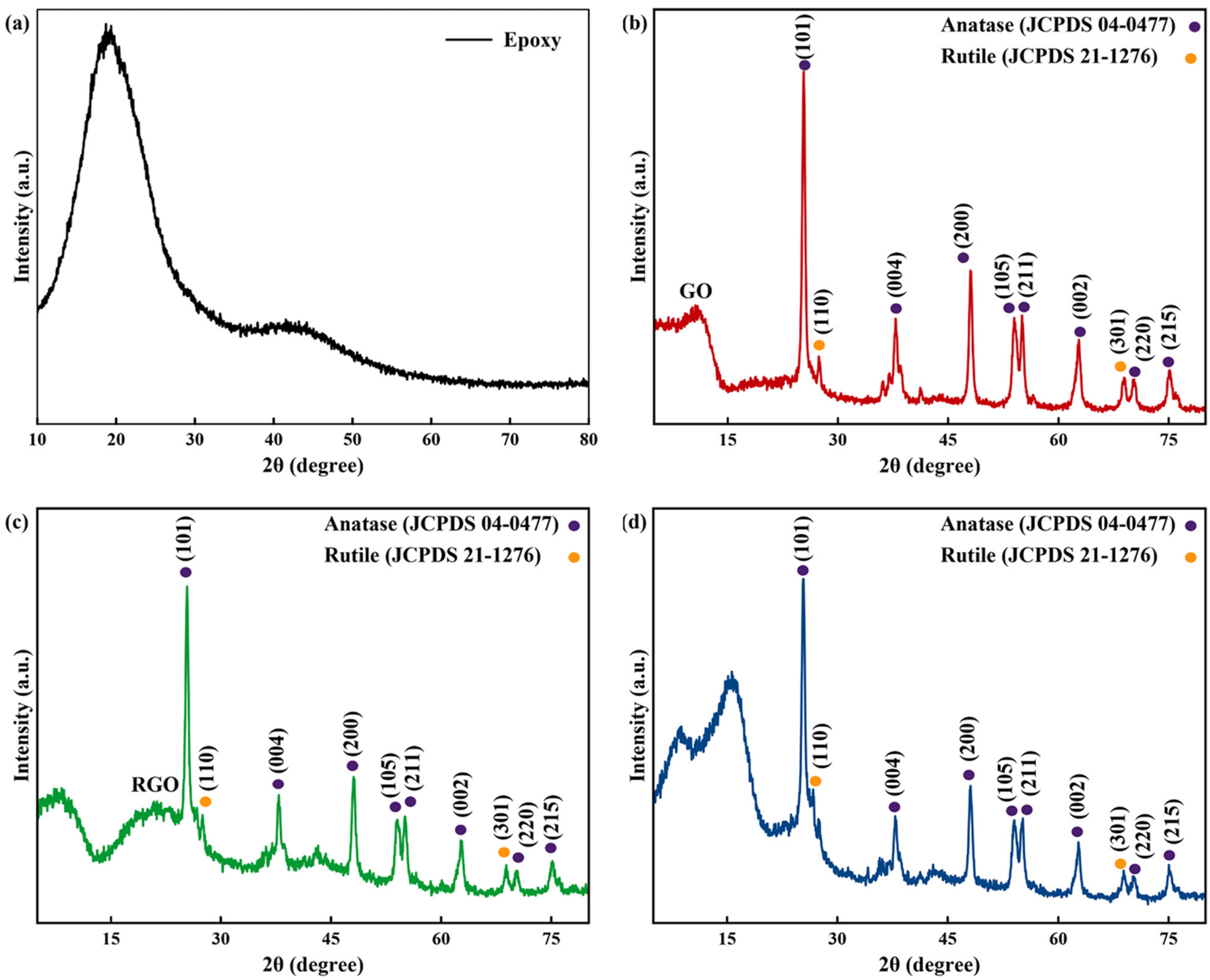

Figure 4: XRD pattern of (a) epoxy, (b) TiO_2/GO (30:70), (c) TiO_2/RGO (30:70), and (d) TiO_2/RGO/epoxy (30:70:50).

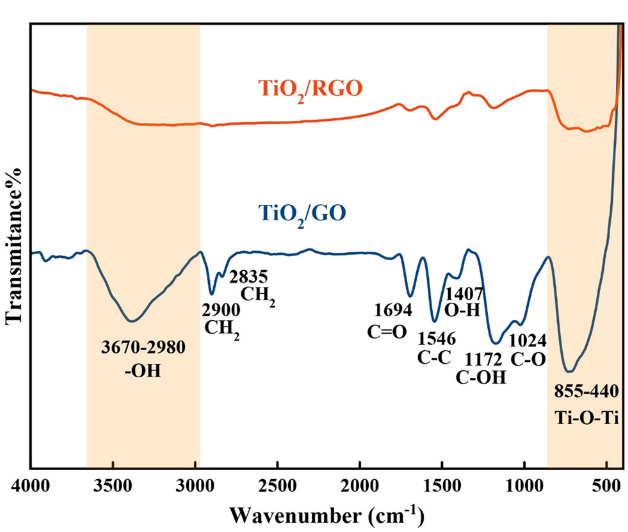

Figure 5: FT-IR spectra of TiO_2/GO (30:70) and TiO_2/RGO (30:70) nanocomposite.

correspond to the vibration mode of C═C and C═O of COOH groups, respectively. The vibration mode of C–O and C–OH also appears at 1,024 and 1,172 cm^{-1}, respectively. In addition, two peaks at 2,900 and 2,835 cm^{-1} can be indexed as a C–H vibration [53,54]. A broad band at 3,670–2,980 cm^{-1} and a weak peak at 1,407 cm^{-1} are imputed to stretching vibrations of OH [55–57]. The FT-IR spectrum of TiO_2/RGO nanocomposite presents weak peaks owing to the decomposition of GO bonds through the synthesis of RGO.

SEM analysis of cured epoxy composites was performed to determine the exfoliation and dispersion of TiO_2 NPs, RGO, and TiO_2/RGO nanocomposite in the matrix. Figure 6 shows the morphology of pure epoxy resin and TiO_2/RGO/epoxy (30:70:50) in different magnifications. A smooth surface of pure epoxy can be clearly seen in Figure 6(a). Figure 6(b)–(d) reveals that TiO_2/RGO forms thin layers as divided sheets with great dispersion in the

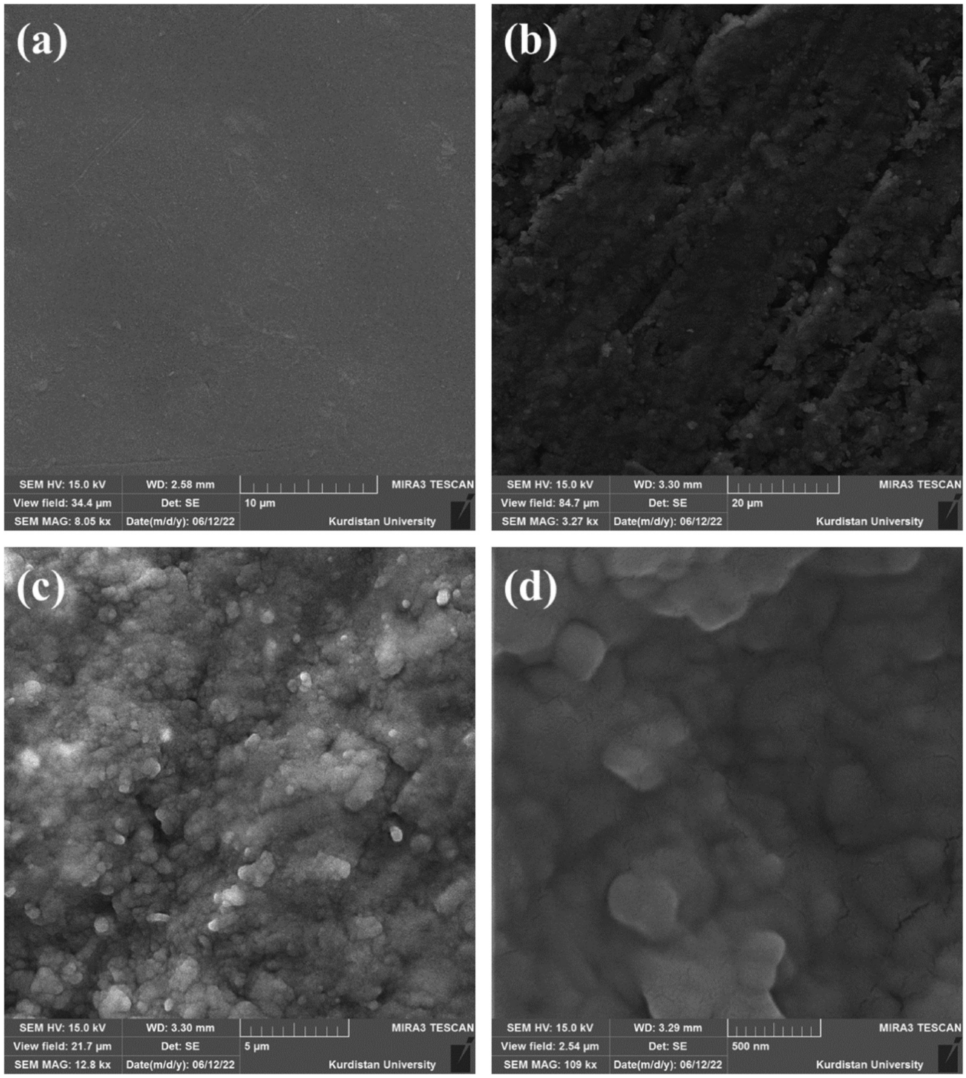

Figure 6: SEM images of (a) pure epoxy and (b)–(d) TiO_2/RGO/epoxy (30:70:50) in different scales.

epoxy matrix. Therefore, this nanofiller in the epoxy resin at 50 wt% can improve epoxy performance.

Furthermore, it is found that the roughness of cured composite epoxy is higher than that of cured pure epoxy and that the cured composite epoxy exhibits more irregular and coarse surface features.

3.2 EM properties of the TiO_2/RGO/epoxy

The RL has strongly pertained to the μ_r and ε_r of the samples, which influence the impedance matching and attenuation characteristics. The microwave absorption features of the samples determine the impedance matching and attenuation characteristics. The impedance matching indicates if the microwave can transmit through the samples, and the

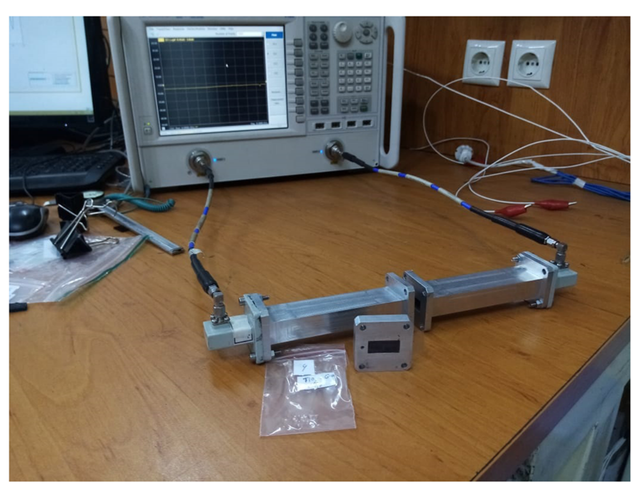

Figure 7: Setup for measuring EM properties of samples by NRW method with microwave network analyzer.

attenuation characteristic is a factor for the evaluation of the ability of the samples toward the conversion of the microwave energy to heat dissipation [39]. Figure 7 shows the NRW method. This setup includes a pair of 3.5 mm coax-to-waveguide adapters, two coaxial cables with SMA connectors, two waveguide standard sections, an N5222A PNA microwave network analyzer, and a waveguide shim. The aperture dimensions of waveguides follow WR-90 rectangular waveguide size. The manufactured samples were placed in the rectangular aperture of the WR-90 waveguide and connected to an N5222A PNA Microwave Network Analyzer. Their S-parameters were measured in the 8.2 to 12.4 GHz frequency range. Therefore, their permittivity and permeability coefficients were calculated using the NRW formula [58] as follows:

$$\mu_r^* = \mu' - j\mu'' = \frac{2\pi}{\Lambda\sqrt{k_0^2 - k_c^2}} \left(\frac{1 + \Gamma}{1 - \Gamma}\right), \tag{11}$$

$$\varepsilon_r^* = \varepsilon' - j\varepsilon'' = \frac{1}{\mu_r^* k_0^2}\left(\frac{4\pi^2}{\Lambda^2} + k_c^2\right), \tag{12}$$

$$\Gamma = X \pm \sqrt{X^2 - 1}, \tag{13}$$

$$X = \frac{S_{11}^2 - S_{21}^2 + 1}{2S_{11}}, \tag{14}$$

$$T = \frac{S_{11} + S_{21} - \Gamma}{1 - (S_{11} + S_{21})\Gamma}, \tag{15}$$

$$\frac{1}{\Lambda^2} = -\left[\frac{1}{2\pi}\ln(T)\right]^2, \tag{16}$$

where S_{ij} is the scattering parameter of the 2-port microwave network; μ_r^* is the relative complex permeability of specimen, ε_r^* is the relative complex permittivity of specimen, $k_0 = \frac{2\pi}{\lambda_0}$ is the wavenumber in free space, $k_c = \frac{2\pi}{a}$ is the waveguide cutoff wavenumber (rad/m); $a = 22.86$ is the width of rectangular waveguide (m) , $\lambda_0 = \frac{c_0}{f}$ is the wavelength in free space (m); c_0 is the speed of light in free space; and f is the measurement frequency (Hz).

The real (ε' and μ') and imaginary (ε'' and μ'') parts of ε_r and μ_r were calculated for the samples, as depicted in Figure 8. The real parts are related to energy storage. In contrast, the imaginary parts are attributed to energy loss for electric/magnetic fields. According to Figure 8(a) and (b), the TiO_2/epoxy is a pure dielectric material and shows almost constant values over the whole frequency range. After the incorporation of the GO and TiO_2 composition into the epoxy matrix, both ε' and ε'' are slightly improved in the frequency range of 8.2–12.4 GHz compared with S1 and S2. However, increasing the TiO_2 content leads to a reduction of the permittivity (S6 and S7). This means that a high TiO_2 percentage leads to a reduction of the dielectric constants. The reduction of GO to RGO enhances both parts of permittivity, leading to the composition of TiO_2, RGO, and epoxy being able to absorb more microwave energy. Adding the TiO_2 and RGO causes more capacitance and increases dielectric constants [59]. Multiple polarization consisting of interfacial and dipole polarization and some remaining oxygen functional groups of GO improve the permittivity [60]. The annealing process improves the graphitization and conductivity of RGO, increasing the real and imaginary parts of the permittivity [61]. Figure 8(c) and (d) illustrates the real and imaginary parts of the permeability in the frequency range of 8.2–12.4 GHz, respectively. The μ' behavior of the samples showed almost constant values around 1 from 8.2 to 12.4 GHz. Among the samples, the maximal microwave magnetic loss value was achieved for S8 in the X-band (8.2–12.4 GHz) frequency. Dielectric loss ($\tan\delta_E = \varepsilon''/\varepsilon'$) and magnetic loss ($\tan\delta_H = \mu''/\mu'$) are depicted in Figure 8(e) and (f). The highest $\tan\delta_E$ can be observed for S7 and S8 over the whole frequency range, suggesting that these specimens are more conducive to microwave absorption. Due to magnetic losses, all samples have low magnetic field attenuation. Therefore, the electric losses are the dominant properties of the proposed samples to design multilayer absorbers.

3.3 Transmission line method and impedance matching optimization

In the case of multilayer absorbers, the number of layers and the total thickness are determined as design constraints. However, the material arrangement and the layer thickness are the variables that create the statistical population. For example, if there are nine types of material to design a 3-layer absorber, the minimum thickness change step is considered equal to 0.1 mm, and the total thickness is determined to be 3 mm maximum, each point has six dimensions $p_i = (n_1, n_2, n_3, t_1, t_2, \text{and } t_3)$. The three primary dimensions are related to the type of material in each layer, each of which has nine possibilities. Furthermore, the other three dimensions are related to the thickness of each layer, which can vary between 0.1 and 3 mm. The RL is calculated for each point using the transmission line theory method in the X-band range for each frequency with a step of 0.01 GHz.

Moreover, the cost function 1 and 2 described below will determine the score of each point for subsequent comparisons. The optimization starts with 50 local groups of 5 people, which are randomly created, and according to the obtained results, the p-best, l-best, and g-best points are identified and stored, and then, they start their movement

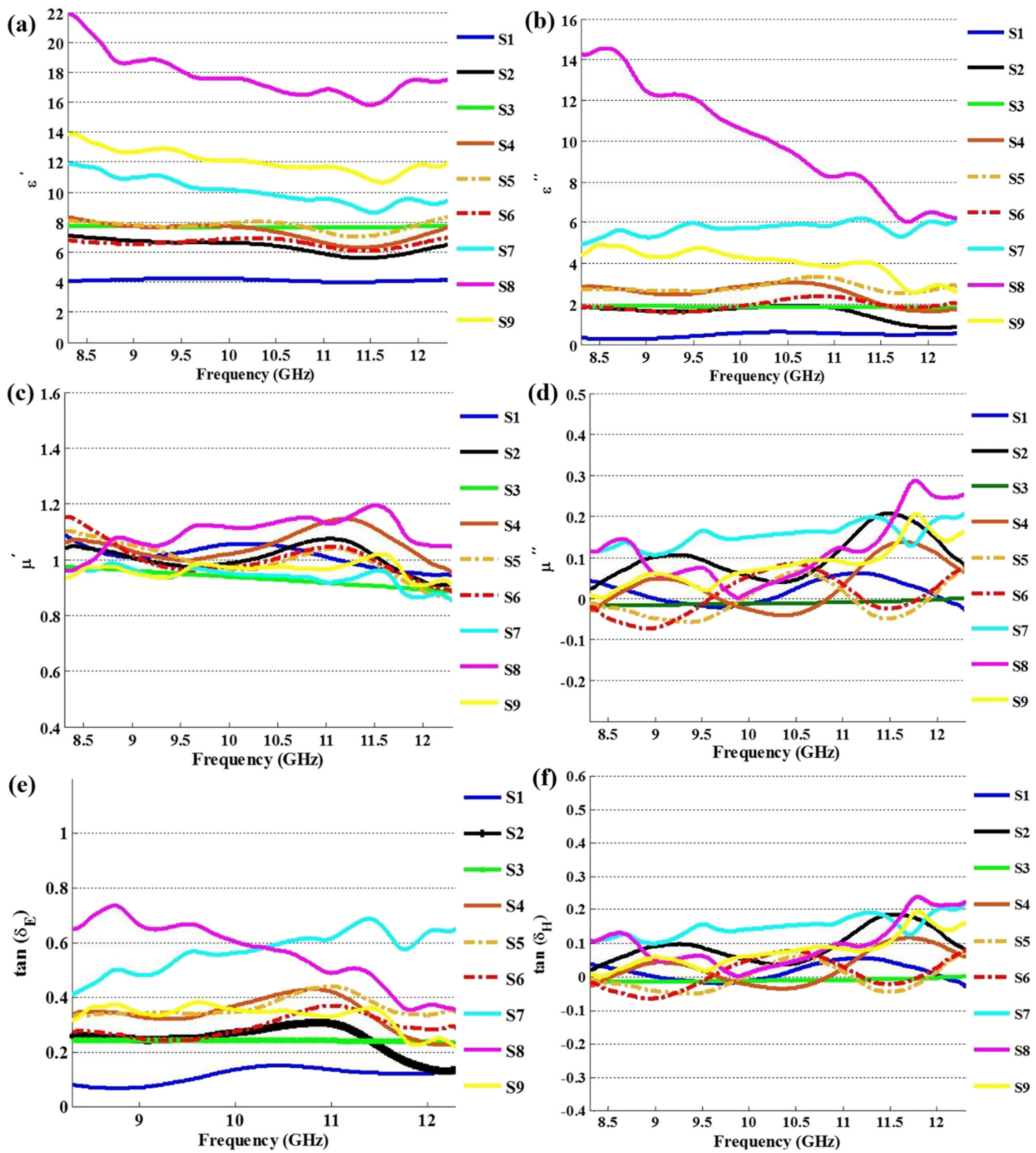

Figure 8: Frequency dependence of (a) and (b) complex permittivity, (c) and (d) complex permeability, (e) dielectric loss, and (f) magnetic loss of samples.

with the described speed and acceleration in the direction of l-best. In each step, p-best, l-best, and g-best are retrieved to identify the best. This operation is repeated until the points are concentrated in g-best, and after the desired convergence in enough iterations, the iteration loop can be ended. Moreover, finally, the best multilayer absorber and its performance will be reported in g-best. Two cost functions were defined as shown in the following: Cost function 1 (to achieve the maximum absorption bandwidth with the lowest RL):

$$\mathrm{cost}_i 1(n_1.\ t_1.\ n_2.\ t_2.\ \cdots\cdots) = \max\{\min_i|\Gamma(f_i)|\}. \quad (17)$$

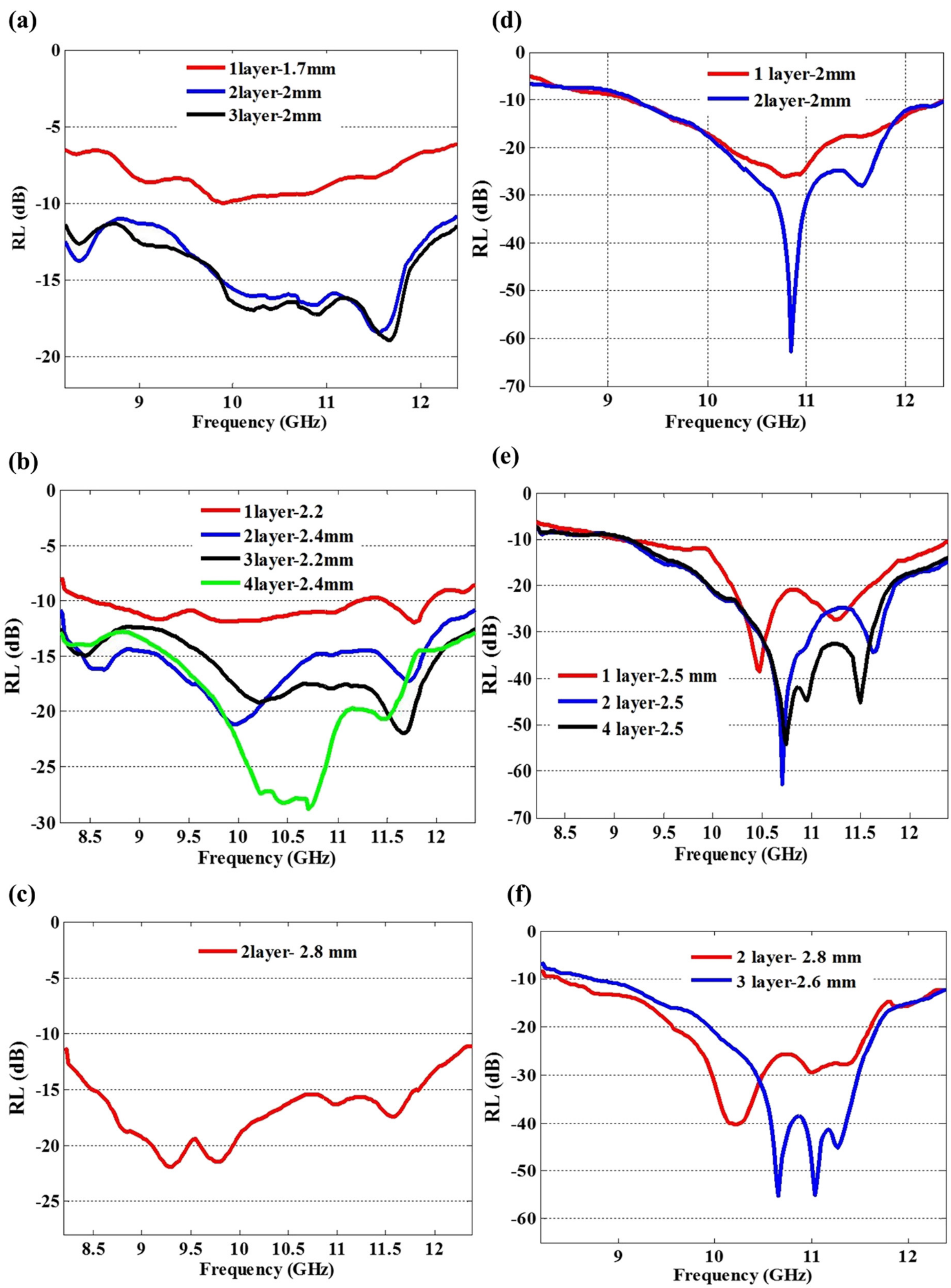

Figure 9: Sample optimization by (a)–(c) cost function 1 and (d)–(f) cost function 2. (a) Cost1–2 mm, (b) Cost1–2.5 mm, (c) Cost1–3 mm, (d) Cost2–2 mm, (e) Cost2–2.5 mm, and (f) Cost2–3 mm.

Table 2: Samples optimized by cost function 1 with limitation of total thickness 2 mm and the number of layers from 1 to 5

N layers	Material in layers	Layer thickness (mm)	Min RL (dB)	Max RL (dB)	Mean RL (dB)	RL <−10 (dB)	RL <−20 (dB)
1 Layer	S8	1.7	−6.15	−9.98	−8.41	—	—
	Total thickness	1.7					
2 Layers	S8	0.5	−10.82	−18.41	−14.23	X band	—
	S6	1.5					
	Total thickness	2					
3 Layers	S8	0.5	−11.33	−18.89	−14.67	X band	—
	S1	0.2					
	S5	1.3					
	Total thickness	2					

Table 3: Samples optimized by cost function 1 with limitation of total thickness 2.5 mm and the number of layers from 1 to 5

N layers	Material in layers	Layer thickness (mm)	Min RL (dB)	Max RL (dB)	Mean RL (dB)	RL< −10 (dB)	RL< −20 (dB)
1 Layer	S7	2.2	−8.07	−11.94	−-10.72	3.2 GHz	—
	Total thickness	2.2					
2 Layers	S8	0.8	−10.82	−21.15	−15.79	X band	0.3 GHz
	S6	1.6					
	Total thickness	2.4					
3 Layers	S8	0.2	−12.35	−21.97	−16.1	X band	0.2 GHz
	S7	0.4					
	S6	1.6					
	Total thickness	2.2					
4 Layers	S8	0.3	−12.81	−28.89	−18.59	X band	1.2 GHz
	S1	0.9					
	S7	0.6					
	S6	0.6					
	Total thickness	2.4					

Table 4: Samples optimized by cost function 1 with limitation of total thickness 3 mm and the number of layers from 1 to 5

N layer	Material in layers	Layer thickness (mm)	Min RL (dB)	Max RL (dB)	Mean RL (dB)	RL< −10 (dB)	RL< −20 (dB)
2 Layers	S2	1.1	−11.13	−21.93	−16.86	X band	0.7 GHz
	S7	1.7					
	Total thickness	2.8					

Table 5: Samples optimized by cost function 2 with limitation of total thickness 2 mm and the number of layers from 1 to 5

N layers	Material in layers	Layer thickness (mm)	Min RL (dB)	Max RL (dB)	Mean RL (dB)	RL< −10 (dB)	RL< −20 (dB)
1 Layer	S9	2	−5.13	−26.1	−15.14	3.2 GHz	1 GHz
	Total thickness	2					
2 Layers	S9	1.3	−6.56	−62.65	−17.90	3.2 GHz	1.6 GHz
	S1	0.7					
	Total thickness	2					

Table 6: Samples optimized by cost function 2 with limitation of total thickness 2.5 mm and the number of layers from 1 to 5

N layers	Material in layers	Layer thickness (mm)	Min RL (dB)	Max RL (dB)	Mean RL (dB)	RL< −10 (dB)	RL< −20 (dB)
1 Layer	S5	2.5	−6.19	−38.55	−16.22	3.5 GHz	1.3 GHz
	Total thickness	2.5					
2 Layers	S7	0.7	−7.59	−62.82	−20.54	3.4 GHz	1.8 GHz
	S1	1.8					
	Total thickness	2.5					
4 Layers	S7	0.5	−7.44	−54.23	−21.66	3.2 GHz	1.6 GHz
	S4	0.4					
	S1	1.4					
	S7	0.2					
	Total thickness	2.5					

At each step with this cost function, the lowest RL value for each member in the entire frequency range is recorded. The best absorption occurs when cost function 1 is maximized. The maximum value recorded in cost1 is stored in p-best, the maximum value in each group is stored in l-best, and the maximum value in all groups is stored in g-best. According to the results recorded in p-best and l-best, the members move toward the target points with the acceleration and speed described previously, and new points are made. The new points are re-evaluated according to the cost function. Therefore, p-best, l-best, and g-best are updated. This iteration continues until the points converge toward g-best. Cost function 2 (to achieve the maximum average RL) was calculated as follows:

$$\text{cost2}(n_1.\ t_1.\ n_2.\ t_2.\ \cdots\cdots) = \frac{\sum_i |\Gamma(f_i)|}{\sum_i 1}. \tag{18}$$

In cost function 2, the average RL at all frequencies is calculated. Any member whose cost2 is higher has a higher value. Like cost function 1, the maximum value recorded in cost2 is stored in p-best, the maximum value in each group is stored in l-best, and the maximum value in all groups is stored in g-best. The rest of the steps will be repeated like cost1.

Table 7: Samples optimized by cost function 2 with limitation of total thickness 3 mm and the number of layers from 1 to 5

N layers	Material in layers	Layer thickness (mm)	Min RL (dB)	Max RL (dB)	Mean RL (dB)	RL< −10 (dB)	RL< −20 (dB)
2 Layers	S2	1.5	−8.41	−40.35	−21.03	4 GHz	2 GHz
	S7	1.3					
	Total thickness	2.8					
3 Layers	S2	0.8	−6.80	−55.18	−22.1	3.5 GHz	1.7 GHz
	S7	0.6					
	S3	1.2					
	Total thickness	2.6					

Table 8: Comparison of the microwave-absorbing properties of different related composites or structures reported in the literature

Materials	Matrix	*d* (mm)	Min RL (dB)	Bandwidth (GHz) (<−10 dB)	Ref.
TiO_2/RGO	Epoxy	2	−62.65	3.2	This work
TiO_2/RGO	Epoxy	2.5	−62.82	3.4	This work
GO-CNTs/epoxy foam	Epoxy	3	−41.5	7.1	[62]
Carbon black and $Ni_{0.6}Zn_{0.4}Fe_2O_4$	Epoxy	2	−24	4.8	[63]
MXene/Fe_3O_4	Wax	2.6	−50.3	1.9	[64]
ZnO/RGO	—	3.2	−67.13	7.44	[65]
[$CaTiO_3$/$ZnFe_2O_4$]@C	Epoxy	2	−22	7.2	[66]
Fe_3O_4/carbon fiber and Fe_3O_4/RGO	Epoxy	2	−52	4	[67]

The cost function, total thickness, and the number of layers are given to the software as design limitations in each optimization. The number of absorption layers is chosen between 1 and 5. Also, the maximum total thickness was determined to be 2, 2.5, and 3 mm. Furthermore, the minimum thickness changes were considered to be 0.1 mm. The four components of permittivity and permeability of the samples are provided to the software as primary data. The cost functions 1 and 2 are used in optimization, as shown in Figure 9. Also, the total absorber thickness is considered to be between 2 and 3 mm. Furthermore, the number of layers is assumed to be between 1 and 5. Used materials and their thickness in optimum multilayer absorbers are listed in Tables 2–7; the arrangement of the layers from top to bottom indicates the order of the layers from the air side to the metal side.

Based on the optimization results, in a single-layer absorber design producer by cost1, sample S7 with a thickness of 2.2 mm has a maximum bandwidth of more than −8.07 dB RL compared to other specimens. For cost2, the maximum average RL equals −16.22 dB for sample S5 with a thickness of 2.5 mm. In our study, increasing the thickness did not improve absorption properties for the single-layer absorber design. In some multilayer absorber design processes, enhancing the number of layers improves absorber's performance. It is shown in Table 3 that when the number of layers increases from 1 to 4, the performance of the designed absorber shows more improvement. Nevertheless, enhancing layer numbers does not improve absorption characteristics in most multilayer absorber design processes. In these cases, the presented optimization software calculates the thickness of one or more layers equal to zero values, as shown in Table 5. This table shows that when cost function 2 is used for optimizing multilayer absorber design with a maximum thickness of 2 mm limitation, a two-layer absorber with a thickness of 2 mm has the best performance, and introduced software automatically considers zero values for the thickness of other absorber layers. Also, the optimized multilayer absorbers, designed by developed software based on increasing the layer numbers and enhancing total thickness limitation, are stated in Tables 2–7. As indicated in Table 3, a 4-layer absorber with a thickness of 2.4 mm, which is designed based on cost function 1, has the best RL bandwidth of less than −12.81 dB compared to other introduced samples. Also, a 3-layer absorber with a thickness of 2.6 mm, which is designed based on cost function 2, has the best result of average RL of about −22.1 dB compared to other specimens, as shown in Table 7.

The material type and layer thickness of multilayer absorbers in optimization with the cost function 2 and the total thickness limitation of 2, 2.5, and 3 mm are summarized in Tables 5–7, respectively.

A comparison of the absorption performance of the synthesized nanocomposites with the reported materials is summarized in Table 8. According to reports, a superior ability to absorb microwave was observed compared with other reports, and the effective absorption was broadened to the whole X band.

4 Conclusion

In this research, TiO_2/RGO/epoxy nanocomposites with a different weight ratio were fabricated using a simple method of annealing followed by magnetic stirring. The SEM images of the nanocomposite exhibited good exfoliation and dispersion of TiO_2/RGO as nanofiller in the epoxy resin. Investigation of the EM properties shows that the annealing process improves the graphitization and conductivity of RGO, increasing the real and imaginary parts of permittivity. The measurement of the EM properties of the prototypes shows small magnetic losses; then, the electric loss is the dominant property for designing of multilayer absorbers.

The optimization algorithm shows that multilayer absorbers perform better than single-layer absorbers with a certain thickness. With cost function 1, the performance of a single layer with a thickness of 2.2 mm, the minimum loss of −8.07 dB reached −12.81 dB in four layers with a thickness of 2.4 mm. With cost function 2, the single-layer absorption with a thickness of 2.5 mm, the average RL of −16.22 dB reached −22.1 dB in three layers with a thickness of 2.6 mm. Therefore, increasing the total thickness and number of layers is effective up to a range.

Acknowledgments: We gratefully acknowledge from the Iranian Nano Council and Bu-Ali Sina University for the support of this work.

Funding information: This work was supported by the Basic Science Research Program through the National Research Foundation of Korea (NRF) funded by the Ministry of Education, Science and Technology (2022R1A2C1004437). It was also supported by the Korea government (MSIT) (2022M3J7A1062940). The authors also gratefully acknowledge the Iranian Nano Council and Bu-Ali Sina University for supporting this work.

Author contributions: Mohammad Reza Karami: conceptualization, methodology, writing – original draft, writing – review and editing, validation, formal analysis. Babak Jaleh: conceptualization, supervision, methodology, writing – original draft, writing – review and editing. Mahtab Eslamipanah: methodology, writing – original draft, writing – review and editing, validation, investigation. Atefeh Nasri: methodology, writing – original draft, writing – review and editing, validation, investigation. Kyong Yop Rhee: writing – original draft, review and editing. All authors have accepted responsibility for the entire content of this manuscript and approved its submission.

Conflict of interest: The authors state no conflict of interest.

Data availability statement: All data generated or analyzed during this study are included in this published article.

References

[1] Li C-B, Li Y-J, Zhao Q, Luo Y, Yang G-Y, Hu Y, et al. Electromagnetic interference shielding of graphene aerogel with layered microstructure fabricated via mechanical compression. ACS Appl Mater. 2020;12(27):30686–94.
[2] Wei Q, Pei S, Qian X, Liu H, Liu Z, Zhang W, et al. Superhigh electromagnetic interference shielding of ultrathin aligned pristine graphene nanosheets film. Adv Mater. 2020;32(14):1907411.
[3] Gareev KG, Bagrets VS, Golubkov VA, Ivanitsa MG, Khmelnitskiy IK, Luchinin VV, et al. Synthesis and characterization of polyaniline-based composites for electromagnetic compatibility of electronic devices. Electronics. 2020;9(5):734.
[4] Soares BG, Barra GMO, Indrusiak T. Conducting polymeric composites based on intrinsically conducting polymers as electromagnetic interference shielding/microwave absorbing materials-A review. J Compos Sci. 2021;5(7):173.
[5] Jiang L, Li X, Zhang J. Design of high performance multilayer microwave absorbers using fast Pareto genetic algorithm. Sci China Ser E-Technol Sci. 2009;52(9):2749–57.
[6] Yang P-A, Huang Y, Li R, Sun Y, Huang X, Shou M, et al. Optimization design and simulation of a light broadband multilayer composite absorber. J Comput Electron. 2021;20(5):1829–39.
[7] Krishna KM, Jain A, Kang HS, Venkatesan M, Shrivastava A, Singh SK. Development of the broadband multilayer absorption materials with genetic algorithm up to 8 GHz Frequency. Secur Commun Netw. 2022;2022:1–12.
[8] Ghanbari F, Moradi Dehaghi S, Mahdavi H. Epoxy-based multilayered coating containing carbon nanotube (CNT), silicon carbide (SiC), and carbonyl iron (CI) particles: as efficient microwave absorbing materials. J Coat Technol Res. 2020;17:815–26.
[9] Yildizel SA, Toktas A. ABC algorithm-based optimization and evaluation of nano carbon black added multi-layer microwave absorbing ultra weight foam concrete. Mater Today Commun. 2022;32:104035.
[10] Yadav R, Panwar R. Effective medium approximation fused optimization strategy derived new kind of honeycomb microwave absorbing structure. IEEE Trans Magn. 2022;58(3):1–11.
[11] Lan C, Zou L, Qiu Y, Ma Y. Tuning solid-air interface of porous graphene paper for enhanced electromagnetic interference shielding. J Mater Sci. 2020;55(15):6598–609.
[12] Gao W, Zhao N, Yu T, Xi J, Mao A, Yuan M, et al. High-efficiency electromagnetic interference shielding realized in nacre-mimetic graphene/polymer composite with extremely low graphene loading. Carbon. 2020;157:570–7.
[13] Sun X, He J, Li G, Tang J, Wang T, Guo Y, et al. Laminated magnetic graphene with enhanced electromagnetic wave absorption properties. J Mater Chem C. 2013;1(4):765–77.
[14] Zhang X, Wang X, Meng F, Chen J, Du S. Broadband and strong electromagnetic wave absorption of epoxy composites filled with ultralow content of non-covalently modified reduced graphene oxides. Carbon. 2019;154:115–24.
[15] Yuan Y, Liu L, Yang M, Zhang T, Xu F, Lin Z, et al. Lightweight, thermally insulating and stiff carbon honeycomb-induced graphene composite foams with a horizontal laminated structure for electromagnetic interference shielding. Carbon. 2017;123:223–32.
[16] Li X, Yang S, Sun J, He P, Pu X, Ding G. Enhanced electromagnetic wave absorption performances of Co_3O_4 nanocube/reduced graphene oxide composite. Synth Met. 2014;194:52–8.
[17] Wang Y, Chen D, Yin X, Xu P, Wu F, He M. Hybrid of MoS_2 and reduced graphene oxide: a lightweight and broadband electromagnetic wave absorber. ACS Appl Mater Interfaces. 2015;7(47):26226–34.
[18] Ding Y, Zhang L, Liao Q, Zhang G, Liu S, Zhang Y. Electromagnetic wave absorption in reduced graphene oxide functionalized with Fe_3O_4/Fe nanorings. Nano Res. 2016;9(7):2018–25.
[19] Majidi S, Jaleh B, Feizi Mohazzab B, Eslamipanah M, Moradi A. Wettability of graphene oxide/zinc oxide nanocomposite on aluminum surface switching by UV irradiation and low temperature annealing. J Inorg Organomet Polym. 2020;30(8):3073–83.
[20] Naghdi S, Jaleh B, Eslamipanah M, Moradi A, Abdollahi M, Einali N, et al. Graphene family, and their hybrid structures for electromagnetic interference shielding applications: Recent trends and prospects. J Alloys Compd. 2022;900:163176.
[21] Jaleh B, Shariati K, Khosravi M, Moradi A, Ghasemi S, Azizian S. Uniform and stable electrophoretic deposition of graphene oxide on steel mesh: Low temperature thermal treatment for switching from superhydrophilicity to superhydrophobicity. Colloids Surf, A Physicochem Eng Asp. 2019;577:323–32.
[22] Zhang L, Yu X, Hu H, Li Y, Wu M, Wang Z, et al. Facile synthesis of iron oxides/reduced graphene oxide composites: application for electromagnetic wave absorption at high temperature. Sci Rep. 2015;5(1):1–9.
[23] Guo A-P, Zhang X-J, Qu J-K, Wang S-W, Zhu J-Q, Wang G-S, et al. Improved microwave absorption and electromagnetic interference shielding properties based on graphene-barium titanate and polyvinylidene fluoride with varying content. Mater Chem Front. 2017;1(12):2519–26.
[24] Kumar R, Dhawan SK, Singh HK, Kaur A. Charge transport mechanism of thermally reduced graphene oxide and their fabrication for high performance shield against electromagnetic pollution. Mater Chem Phys. 2016;180:413–21.
[25] Mohanapriya MK, Deshmukh K, Kadlec J, Sadasivuni KK, Faisal M, Nambi Raj NA, et al. Dynamic mechanical analysis and broadband electromagnetic interference shielding characteristics of poly (vinyl alcohol)-poly (4-styrenesulfonic acid)-titanium dioxide nanoparticles based tertiary nanocomposites. Polym-Plast Tech Mat. 2020;59(8):847–63.
[26] Harish Kumar A, Ahamed MB, Deshmukh K, Sirajuddeen MS. Morphology, dielectric and EMI shielding characteristics of graphene nanoplatelets, montmorillonite nanoclay and titanium dioxide nanoparticles reinforced polyvinylidenefluoride nanocomposites. J Inorg Organomet Polym. 2021;31(5):2003–16.

[27] Mohammed J. Structural, optical, and X-band electromagnetic characterization of composite of TiO_2@Carbon-Fibers@$Srfe_{12}O_{19}$ anchored on polyaniline.

[28] Gao X, Wang B, Wang K, Xu S, Liu S, Liu X, et al. Design of $Ti_3C_2T_x$/TiO_2/PANI multi-layer composites for excellent electromagnetic wave absorption performance. J Colloid Interface Sci. 2021;583:510–21.

[29] Wu H, Qu S, Lin K, Qing Y, Wang L, Fan Y, et al. Enhanced low-frequency microwave absorbing property of SCFs@TiO_2 composite. Powder Technol. 2018;333:153–9.

[30] Yang Z, Ren W, Zhu L, Qing Y, Huang Z, Luo F, et al. Electromagnetic-wave absorption property of Cr_2O_3-TiO_2. coating with frequency selective surface J Alloys Compd. 2019;803:111–7.

[31] Wang D, Tan D, Liu L. Particle swarm optimization algorithm: an overview. Soft Comput. 2018;22(2):387–408.

[32] Basu M. Modified particle swarm optimization for nonconvex economic dispatch problems. Int J Electr Power Energy Syst. 2015;69:304–12.

[33] Chamaani S, Mirtaheri SA, Shooredeli MA. Design of very thin wide band absorbers using modified local best particle swarm optimization. AEU- Int J Electron Commun. 2008;62(7):549–56.

[34] Joy V, Padwal V, Nair RU, Singh H. Optimal Design of Multi-layered Radar Absorbing Structures (RAS) using Swarm Intelligence based Algorithm. Def Sci J. 2022;72(2):236–42.

[35] He L, Li X, Zhao Y, Zhong Z, Zhang J, Yang Y, et al. The multilayer structure design of magnetic-carbon composite for ultra-broadband microwave absorption via PSO algorithm. J Alloys Compd. 2022;913:165088.

[36] Hummers Jr WS, Offeman RE. Preparation of graphitic oxide. J Am Chem Soc. 1958;80(6):1339.

[37] Shen Q, Shi W-M, Kong W, Ye B-X. A combination of modified particle swarm optimization algorithm and support vector machine for gene selection and tumor classification. Talanta. 2007;71(4):1679–83.

[38] Lee S, Soak S, Oh S, Pedrycz W, Jeon M. Modified binary particle swarm optimization. Prog Nat Sci. 2008;18(9):1161–6.

[39] Chen W, Zheng X, He X, Su Y, Wang J, Yang J, et al. Achieving full effective microwave absorption in X band by double-layered design of glass fiber epoxy composites containing MWCNTs and Fe_3O_4 NPs. Polym Test. 2020;86:106448.

[40] Huang X, Zhang J, Lai M, Sang T. Preparation and microwave absorption mechanisms of the NiZn ferrite nanofibers. J Alloys Compd. 2015;627:367–73.

[41] Schelkunoff SA. The electromagnetic theory of coaxial transmission lines and cylindrical shields. Bell Syst Tech J. 1934;13(4):532–79.

[42] Schulz RB, Plantz VC, Brush DR. Shielding theory and practice. IEEE Trans Electromagn Compat. 1988;30(3):187–201.

[43] Pozar DM. Microwave Engineering. 4th edn. United States of America: John Wiley & Sons; 2011.

[44] Liu H, Meng X, Yang X, Jing M, Shen X, Dong M. Three-layer structure microwave absorbers based on nanocrystalline α-Fe,$Fe_{0.2}(Co_{0.2}Ni_{0.8})_{0.8}$ and $Ni_{0.5}Zn_{0.5}Fe_2O_4$ porous microfibers. J Nanosci Nanotechnol. 2014;14(4):2878–84.

[45] García E, Amaya I, Correa R. Design of an optimal multilayer electromagnetic absorber through Spiral Algorithm. Ing Univ. 2016;20(1):85–118.

[46] Zeinali M, Jaleh B, Rashidian Vaziri MR, Omidvar A. Study of nonlinear optical properties of TiO_2-polystyrene nanocomposite films. Quantum Electron. 2019;49(10):951.

[47] Venkateswarlu K, Bose AC, Rameshbabu N. X-ray peak broadening studies of nanocrystalline hydroxyapatite by Williamson-Hall analysis. Physica B: Condensed Matter. 2010;405(20):4256–61.

[48] Khamboonrueang D, Srirattanapibul S, Tang I-M, Thongmee S. TiO_2•rGO nanocomposite as a photo catalyst for the reduction of Cr^{6+}. Mater Res Bull. 2018;107:236–41.

[49] Zheng P, Liu T, Su Y, Zhang L, Guo S. TiO_2 nanotubes wrapped with reduced graphene oxide as a high-performance anode material for lithium-ion batteries. Sci Rep. 2016;6:36580.

[50] Sheha E. Studies on TiO_2/reduced graphene oxide composites as cathode materials for magnesium-ion battery. Graphene. 2014;2014(3):1–8.

[51] Gohari G, Mohammadi A, Akbari A, Panahirad S, Dadpour MR, Fotopoulos V, et al. Titanium dioxide nanoparticles (TiO_2 NPs) promote growth and ameliorate salinity stress effects on essential oil profile and biochemical attributes of *Dracocephalum moldavica*. Sci Rep. 2020;10(1):1–14.

[52] Jaleh B, Zare E, Azizian S, Qanati O, Nasrollahzadeh M, Varma RS. Preparation and characterization of polyvinylpyrrolidone/polysulfone ultrafiltration membrane modified by graphene oxide and titanium dioxide for enhancing hydrophilicity and antifouling properties. J Inorg Organomet Polym Mater. 2020;30(6):2213–23.

[53] Sagadevan S, Pal K, Koteeswari P, Subashini A. Synthesis and characterization of TiO_2/graphene oxide nanocomposite. J Mater Sci Mater Electron. 2017;28(11):7892–8.

[54] Ruidíaz-Martínez M, Álvarez MA, López-Ramón MV, Cruz-Quesada G, Rivera-Utrilla J, Sánchez-Polo M. Hydrothermal synthesis of rGO-TiO_2 composites as high-performance UV photocatalysts for ethylparaben degradation. Catalysts. 2020;10(5):520.

[55] Ossonon BD, Bélanger D. Synthesis and characterization of sulfophenyl-functionalized reduced graphene oxide sheets. RSC Adv. 2017;7(44):27224–34.

[56] Naghdi S, Jaleh B, Shahbazi N. Reversible wettability conversion of electrodeposited graphene oxide/titania nanocomposite coating: Investigation of surface structures. Appl Surf Sci. 2016;368:409–16.

[57] Liu G, Wang R, Liu H, Han K, Cui H, Ye H. Highly dispersive nano-TiO_2 in situ growing on functional graphene with high photocatalytic activity. J Nanopart Res. 2016;2016(18):1–8.

[58] Tester PA. Standard Test Method for Measuring Relative Complex Permittivity and Relative Magnetic Permeability of Solid Materials at Microwave Frequencies. PA, USA. West Conshohocken: ASTM International; 2022. p. 10

[59] Tong W, Zhang Y, Yu L, Lv F, Liu L, Zhang Q, et al. Amorphous TiO_2-coated reduced graphene oxide hybrid nanostructures for polymer composites with low dielectric loss. Chem Phys Lett. 2015;638:43–6.

[60] Wang Y, Gao X, Wu X, Zhang W, Wang Q, Luo C. Hierarchical $ZnFe_2O_4$@RGO@CuS composite: strong absorption and wide-frequency absorption properties. Ceram Int. 2018;44(8):9816–22.

[61] Fang Y, Wang W, Wang S, Hou X, Xue W, Zhao R. A quantitative permittivity model for designing electromagnetic wave absorption materials with conduction loss: A case study with microwave-reduced graphene oxide. Chem Eng J. 2022;439:135672.

[62] Liu Y, He D, Dubrunfaut O, Zhang A, Zhang H, Pichon L, et al. GO-CNTs hybrids reinforced epoxy composites with porous structure as microwave absorbers. Compos Sci Technol. 2020;200:108450.

[63] Ibrahim IR, Matori KA, Ismail I, Awang Z, Rusly SNA, Nazlan R, et al. A study on microwave absorption properties of carbon black and $Ni_{0.6}Zn_{0.4}Fe_2O_4$ nanocomposites by tuning the matching-absorbing layer structures. Sci Rep. 2020;10(1):3135.

[64] Liu P, Chen S, Yao M, Yao Z, Ng VMH, Zhou J, et al. Double-layer absorbers based on hierarchical MXene composites for microwave absorption through optimal combination. J Mater Res. 2020;35(11):1481–91.
[65] Bao S, Hou T, Tan Q, Kong X, Cao H, He M, et al. Immobilization of zinc oxide nanoparticles on graphene sheets for lithium ion storage and electromagnetic microwave absorption. Mater Chem Phys. 2020;245:122766.
[66] Cai W, Elveny M, Akhtar MN. Enhanced X-band wave dissipation performance in bilayer absorber composed of bare epoxy resin and epoxy resin filled with [$CaTiO_3$/$ZnFe_2O_4$]@C nanocomposite. J Magn Magn Mater. 2021;539:168385.
[67] Gang Q, Akhtar MN, Boudaghi R. Development of high-efficient double layer microwave absorber based on Fe_3O_4/carbon fiber and Fe_3O_4/rGO. J Magn Magn Mater. 2021;537:168181.